Journal of Hazardous Materials 162 (2009) 1111–1120

Contents lists available at ScienceDirect

Journal of Hazardous Materials

journal homepage: www.elsevier.com/locate/jhazmat

Simulation study on the use of strippable coatings for radiocesium decontamination of concrete

Min Tan[a], John D. Whitaker[b], Daniel T. Schwartz[a,*]

[a] Department of Chemical Engineering, University of Washington, Box 351750, Seattle, WA 98195-1750, United States
[b] Isotron R&D Center, 1443N. Northlake Way, Seattle, WA 98103, United States

ARTICLE INFO

Article history:
Received 2 October 2007
Received in revised form 8 April 2008
Accepted 30 May 2008
Available online 7 June 2008

Keywords:
Simulation
Decontamination
Dirty bomb
Radiological dispersion device
Radionuclide

ABSTRACT

The contamination and decontamination of concrete by a soluble contaminant (radiocesium) was modeled using the finite element method. The decontamination process relied on the application of a hyper-accumulating strippable polymer (HASP) to sequester contaminant that was transported to the concrete surface. The model accounted for the transport of cesium by diffusion, capillary pressure-driven convection, and equilibrium adsorption of cesium within the concrete substrate and HASP coating. The influence of HASP properties (porosity, thickness, and cesium distribution coefficient), and a wide range of operation variables (HASP contact time, delay time until HASP decontamination begins, influence of evaporative boundary conditions) on final decontamination efficacy were explored. Transient saturation (moisture content) and cesium concentration profiles were used to understand key factors in the decontamination process, and water wicking experiments were performed to validate the capillary convection model. The results showed that prompt HASP application after the initial contamination event is critical for high decontamination efficacies. A 30-day HASP treatment removed about 90% of the contaminant when HASP was applied within 30 min of the initial contamination event, whereas the decontamination process removed less than half as much cesium if months were allowed to elapse months prior to decontamination. Multiple applications of fresh HASP were also shown to improve decontamination performance under certain circumstances.

1. Introduction

The threat of an attack by radiological dispersion devices (RDD), or "dirty bombs," has prompted concerns about contamination of civil and military infrastructure [1]. Decontamination that permits the infrastructure to be recovered and reused requires nondestructive methods that quickly reduce radiation levels to meet public safety requirements [1–3]. The requirements for remediation and reuse of infrastructure are quite different from the typical strategies used to decontaminate and decommission (D&D) old nuclear facilities [4,5]. For example, RDD contaminated infrastructure may include priceless historic landmarks, precluding demolition-based remediation. More broadly, avoiding demolition is a key strategy for mitigating economic losses on the affected communities and reducing the risk of further contaminant dispersal through the generated airborne dust. Finally, standard D&D methods [6] are designed for concentrated, decades-old radioactive contamination, and only recently have researchers begun to focus on the unique remediation issues associated with the emerging RDD threat [7].

DARPA's (Defense Advanced Research Projects Agency) Radiation Decontamination Program was established to investigate and optimize decontamination techniques specifically tailored to RDD incident response. Our team investigated strippable coatings as a method well suited to the RDD response scenario [8]. Strippable coatings – often applied in the form of non-toxic polymer emulsions – have long been used to physically trap and remove particulate contaminants such as asbestos [9]. Here we develop numerical models to see if this concept can be extended to other forms of contamination by including, within the strippable coating, chemical 'traps' or tight-binding sites, which specifically accumulate one or more target contaminants [8]. These hyper-accumulating strippable polymers, or HASPs, serve three principal functions. First, they are applied (e.g. sprayed or brushed) as liquid, and therefore provide a medium which solvates and transports contamination. Second, their polymer/solid phases reside on the surface and possess very large equilibrium distribution coefficient (K_d) values, providing a sink for contaminants, thereby allowing diffusion out of the subsurface. Third, they cure to an elastomeric solid film,

* Corresponding author. Tel.: +1 206 543 8388; fax: +1 206 685 3451.
E-mail address: dts@u.washington.edu (D.T. Schwartz).

0304-3894/$ – see front matter © 2008 Elsevier B.V. All rights reserved.
doi:10.1016/j.jhazmat.2008.05.153

facilitating removal and transportation. There are several organic and inorganic materials that possess large K_d values, though we have fairly extensive experimental experience with nickel hexacyanoferrates [10–13].

This study explores some of the physical, chemical, and operational parameters that affect remediation of cesium contaminated concrete using HASPs. Cesium-137 was chosen for its combination of availability and toxicity, making it one of the most likely isotopes for use in RDDs [14]. Previous models have simulated the transport of ionic radiocontaminants through the pores of concrete and simulation results were in good agreement with experimental data [15,16]. However, these models typically neglect cesium convection driven by capillary pressure by assuming the concrete is fully saturated. Therefore, developing a mass transport model that also accounts for cesium convection should more accurately reflect reality when a wet contaminant or wet coating is applied to partially saturated concrete. The model can be used to guide and optimize the decontamination process, the design of HASP, and aid decision-making in case of a RDD event.

2. Model formulation

Cesium transport in building substrates (e.g. concrete, marble, granite) is influenced by moisture and ion transport in unsaturated porous media. Here we need to describe unsaturated flow of liquid water through porous concrete whose void space contains ambient air. We assume that the transport of liquid in the partially saturated concrete obeys Darcy's law, with the further assumption that pressure gradients in the gas phase are negligible. With these assumptions, the 1D form of Darcy's law is

$$V_w = -\frac{(k_w/\mu_w)(\partial P_c/\partial S_w)(\partial S_w/\partial x)}{nS_w} \quad (1)$$

where V_w (m/s) is the flow rate of the liquid water phase, P_c (Pa) is the capillary pressure which is defined as the difference between pressures of air phase and water phase, k_w (m^2) is the permeability of water phase, μ_w (Pa s) is the viscosity of water-phase, S_w is the saturation of water phase, n is the porosity of the porous material, x (m) is the independent space variable measuring the depth into the building material from the surface.

Substituting Eq. (1) into the equation of mass conservation [17] for incompressible water in the porous media results in

$$\frac{\partial((k_w/\mu_w)(dP_c/dS_w)(\partial S_w/\partial x))}{\partial x} + n\frac{\partial S_w}{\partial t} = 0 \quad (2)$$

where t is time (s).

Transient mass transport of a dilute chemical species through the porous media is controlled by convection, diffusion and adsorption [17].

$$\frac{\partial S_w C}{\partial t} = -\nabla \cdot S_w(CV_w - D \cdot \nabla C) - \frac{1-n}{n} S\rho_s \frac{\partial F}{\partial t} \quad (3)$$

where C is the concentration of the soluble species (kg/m^3, mass of component per unit volume of fluid), D is the diffusivity of the species in the liquid (m^2/s), S is the specific surface area of the substrate (m^2/kg) and ρ_s is the density of the porous media (kg/m^3 of total volume). V_w is found by solving Eq. (2) and substituting the solution into Eq. (1). Eq. (3) assumes local adsorption equilibrium of species (cesium ions) with F being the adsorption isotherm (moles of surface adsorbed species, mol/m^2).

A key feature of unsaturated flow problems is identifying effective permeability and capillary pressure. The effective permeability and capillary pressure are both functions of saturation, and are greatly affected by the liquid's ability to wet the solid material comprising the porous medium. The system behavior, thus, depends on both the liquid (water, here) and solid (concrete) under study. The expressions for k_w was taken from Corey [18]:

$$k_w = k_{ws}(S_{we})^4 \quad (4)$$

where k_{ws} is the absolute permeability and is independent of saturation. S_{we} is the effective saturation, defined as

$$S_{we} = \frac{S_w - S_{w0}}{1 - S_{w0} - S_{n0}} \quad (5)$$

where S_{w0} and S_{n0} are the medium's residual water and air saturation, respectively. The capillary pressure-saturation relation employed in these simulations is a form proposed by Narasimhan et al. [19]

$$P_c = p_i - p_j\left(\frac{1-S_w}{S_w}\right)^{1/\gamma} \quad (6)$$

where p_i, p_j, and γ are all fitted constants for the particular fluid phases and solid (given later). For the diffusion of cesium ions, a linear relationship ($D = D_s S_w$) between saturation and diffusivity was used where D_s is the diffusivity of the species in fully saturated porous material. For the adsorption of cesium ions, a Langmuir adsorption isotherm was adopted in all simulations:

$$F = \frac{n_0 C K_d}{1 + C K_d} \quad (7)$$

where n_0 is the surface concentration of adsorption sites in mol/m^2, and K_d is the distribution coefficient in m^3/mol. If $C \ll 1/K_d$, then Eq. (7) can be simplified to the linear form

$$F = n_0 C K_d \quad (8)$$

By combining Eqs. (3) and (8), the final governing equation describing the species transport driven by capillary flow, diffusion and adsorption becomes:

$$\left(S_w + \frac{1-n}{n}\rho_s S n_0 K_d\right)\frac{\partial C}{\partial t} = -S_w\nabla \cdot CV_w + \nabla \cdot S_w(D \cdot \nabla C) \quad (9)$$

Therefore, the concentration profiles of the contaminant inside the porous media can be obtained by solving the governing equations for unsaturated flow (Eq. (2)) and the contaminant mole balance (Eq. (9)).

3. Discussion on model inputs

3.1. Model inputs and their sources

All model inputs were either collected experimentally or, where available, obtained from the open literature. In cases where no data was available, reasonable parameters and properties were assumed in an attempt to bound the problem. The assumption that the HASP has the same transport properties as concrete except porosity and distribution coefficient is one example; this particular assumption represents an upper bound on the permeability and capillary pressure relationships for the strippable polymer. Table 1 shows our compilation of the data, their sources, and any specific assumptions made.

3.2. Experiments and simulations of water transport in concrete samples

3.2.1. Wicking experiment method

Parameters presented in Table 1 for the capillary function $P_c(S_w)$ (Eq. (6)) and permeability function $k_w(S_w)$ (Eq. (4)) were measured by Mayer et al. [20] for concrete. The saturated permeability k_{ws} was measured directly for cores drilled from concrete

Table 1
Parameters used in this modeling work

Parameters		Value and unit	Reference
k_{ws}	Saturated permeability	6×10^{-18} m^2	[a]
S_{w0}	Residual water saturation	0.1	[b]
S_{n0}	Residual air saturation	0.2	[20]
D_s	Saturated diffusion coefficient	2×10^{-10} m^2/s	[a] [26]
P_i	Fitted constant	1×10^5 Pa	[20]
P_j	Fitted constant	1.2×10^6 pa	[20]
γ	Fitted constant	1.3	[20]
K_d	Distribution coefficient in concrete	0.00548 m^3/mol	[c]
$K_{d,HASP}$	Distribution coefficient in HASP	0.00137–137 m^3/mol	[d]
S	Specific area	8000 m^2/kg	[27]
n_0	Surface concentration of adsorption sites	3.33×10^{-4} mol/m^2	[28]
n	Porosity of concrete	0.1	[a]
n_{HASP}	Porosity of HASP	0.1, 0.5 and 0.8	[e]
h	Mass transfer coefficient at concrete surface	1×10^{-6} m/s	[25]
ρ_s	Bulk density of concrete	2500 kg/m^3	
μ_w	Viscosity of water	1×10^{-3} Pa s	

[a] ASTM D6527.
[b] Literature [20] value of S_{w0} is 0.3; we used a value consistent with a dry building.
[c] Batch adsorption results using ground concrete, cesium-133, and atomic absorption.
[d] Batch adsorption results, using HASP, cesium-133, and atomic adsorption, Experimental value of $K_{d,HASP}$ is 1.37 m^3/mol, and this value was used unless specified otherwise.
[e] HASP was assumed to have a porosity of 0.5 unless specified otherwise.

coupons provided by DARPA using ASTM D6527 (UFA Ventures). To confirm the validity of the resulting $P_c \sim S_w \sim k_w$ relationship, water-wicking experiments were performed using a Krüss K100 Tensiometer. Samples were diamond-cored from DARPA concrete coupons and measured 1.59 cm in diameter and 2.5–3 cm in length. Each concrete sample was fixed in a custom-made sample holder and suspended from the tensiometer balance. A height-adjustable liquid vessel was used to bring the water into contact with the concrete sample. In this method, water was raised until contact with the concrete sample surface. The weight of the sample was recorded over a 5000 s period. Upon contact, the formation of a macroscopic liquid meniscus at the bottom perimeter of the concrete caused an immediate jump in the apparent mass of the sample, after which the increase in mass was due to water wicking into the concrete pores. Therefore, the mass of water absorbed was obtained by subtracting the external wetting force from the total recorded force. Buoyancy effects were neglected. The temperature at which the measurements were performed was 20 ± 3 °C.

3.2.2. Wicking results and discussions

Fig. 1(a) shows the water uptake data for a series of concrete samples (Fig. 1(b)), as well as simulation results using the literature property values for water in concrete (Table 1). The data is plotted vs. $t^{1/2}$ to display Lucas-Washburn behavior [21,22], which is the expected behavior if the capillary diffusion coefficient [23,24]

$$D_c = -\frac{k_w}{\mu_w}\frac{dP_c}{dS_w} \tag{10}$$

is nearly a constant at an average value denoted $D_{c,ave}$. Under these conditions the mass uptake (m) into a semi-infinite sample is:

$$m = \frac{2\rho_w A_c \sqrt{nD_{c,ave}t}}{\sqrt{\pi}} \tag{11}$$

where ρ_w is the density of water and A_c is the cross-section area of the concrete sample. Here we calculate $D_{c,ave}$ using properties determined at $S_w = 0.45$. Inserting $D_{c,ave} = 1.9 \times 10^{-9}$ m^2/s into Eq. (11), we calculated the slope, $m/\sqrt{t}$, as 0.0031 g/s$^{0.5}$. The best-

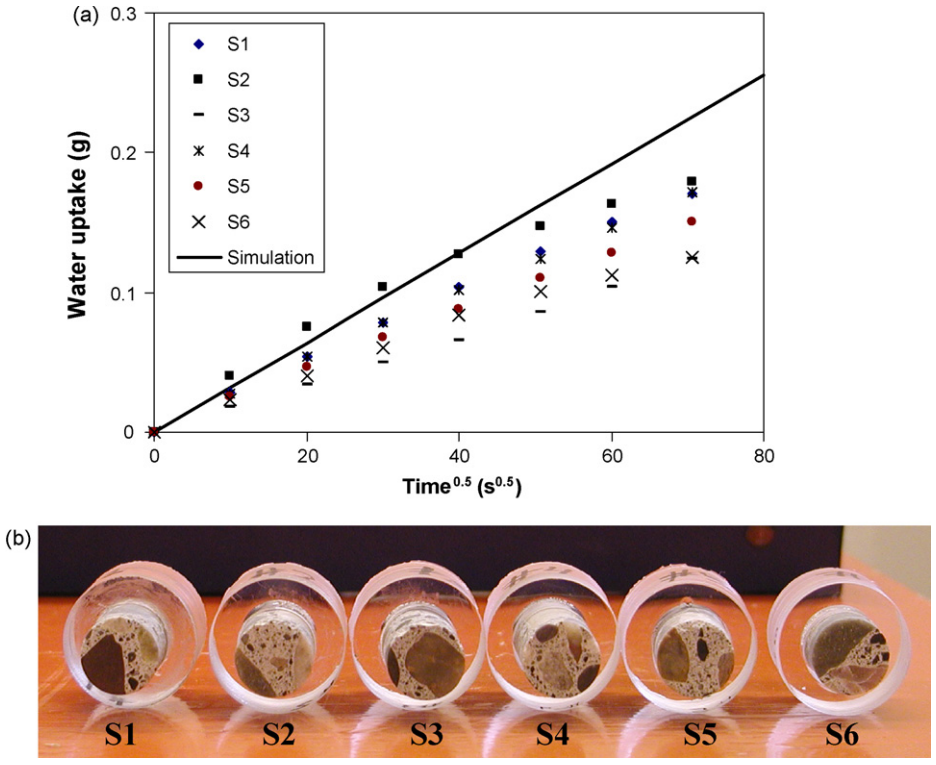

Fig. 1. (a) Comparison of the simulation and experimental water wicking measurements. (b) Pictures of concrete samples used in wicking experiments.

fit slope obtained from the numerical simulation (solid curve in Fig. 1(a)) is 0.0032 g/s$^{1/2}$ when none of the assumptions above are made.

The experimental water wicking data points for the actual concrete samples being used are the symbols plotted in Fig. 1(a). If these data points are fit over the period from 0 s to 3600 s, the average slope $m/\sqrt{t}$ for the six datasets is 0.0021 g/s$^{0.5}$, which is 34% lower than the simulation value of 0.0032 g/s$^{0.5}$. Since the slope of these curves convolute the $P_c \sim S_w$ relationship and the $k_w \sim S_w$ relationship into a single overall wicking response, deviations between experiments and simulation cannot be isolated to uncertainties in the capillary pressure or relative permeability, or both. As a result, we have opted to use the results in Table 1 where the $P_c \sim S_w \sim k_r$ relationships has been measured/estimated independently. Nonetheless, the experiments and simulation in Fig. 1 show that the values in Table 1 provide a reasonable representation of the specific concrete samples used in the experimental portion of this program, though our simulations may slightly overpredict convection in those samples.

4. Simulations and discussions of contamination and decontamination scenario

4.1. Description of contamination and decontamination scenario

Simulations based on the governing equations in Section 2 were performed using FEMLAB 3.1a to model a simple three-step contamination-decontamination scenario, shown sequentially in Fig. 2. Different sets of boundary and initial conditions were defined in each step of the process.

Step 1 involves the contamination of concrete with low residual moisture by a wet contaminant. At time 0, a fixed volume per area (133 ml/m^2) of aqueous solution containing the putative radiocesium contaminant is dispersed on the concrete surface. At the process time of t_{wick}, the volume of liquid completely wicks into the substrate. In all scenarios simulated here, we assume decontamination operators arrive at the scene after t_{wick}. Since Cs^+ has a strong affinity for concrete, it is expected that the penetration rate of Cs^+ is far slower than that of moisture. During Step 2, the contaminant solution inside the substrate is allowed to dry for t_{dry} under conditions where evaporation from the exposed concrete surface takes place into the ambient environment. In the drying step, part of the liquid that penetrates into the substrate in the first step is removed, reducing the overall saturation in the pores. Contaminant (Cs^+) is not removed by evaporation, but continues to redistribute within the building material. Drying time is one of the most significant variables in this process, and is dictated by how quickly a response team can reach the site of contamination. Step 3 begins at the process time of $t_{wick} + t_{dry}$, when a liquid film of HASP is applied to the contaminated concrete surface. The concrete is allowed to decontaminate for a duration denoted t_{decon}. How long the HASP resides on the surface before stripping and disposing is another important process variable. The HASP surface is either exposed to the ambient environment where evaporation can occur, or covered by a barrier film to prevent evaporation. During this step, contaminant is transported from the concrete substrate to the HASP layer, and the HASP cures until it forms a solid coating that can be stripped off the surface and disposed.

We describe simulation results that evaluate the influence of these various process variables. The first part is to show one specific contamination/decontamination scenario in detail, step-by-step. Then, we elaborate on the impact of various process options that influence the overall decontamination efficacy.

4.2. Simulation study of one complete contamination and decontamination process

4.2.1. Step 1: apply Cs^+ as aqueous solution (contamination step)

Upon application of 133 ml/m^2 of contaminant solution, simulation shows that t_{wick} = 69 s for the concrete properties presented in Table 1, assuming the material had an initial concrete saturation of $S_w = S_{w0} = 0.1$. The wet surface at $t = 0$ and $x = 0$ was assumed to have a saturation of $S_w = 1 - S_{n0} = 0.8$ during the entire wick-in period. The concrete was assumed to be deep compared to the fluid penetration depth (in simulations, this was accomplished by fixing a distant point in the solid at the initial moisture content, $S_w = S_{w0} = 0.1$). For cesium ion transport, we further assumed that the initial material is uncontaminated, and the contaminant concentration at concrete surface ($x = 0$) remains at the solution concentration (C_0) during the contamination step, i.e., $C/C_0 = 1$ at $x = 0$ and the concentration far from the surface remains at the initial, uncontaminated state.

Fig. 3 shows the moisture (Fig. 3(a)) and the concentration (Fig. 3(b)) profiles in the substrate (0 m < x < 0.01 m) after applying a wet layer of cesium-containing solution at the concrete surface. At t = 69 s, the moisture penetration depth (2.6 mm) is more than 100 times larger than the Cs^+ penetration depth (0.022 mm). As a result of adsorption to the concrete, most contaminant stays close to the concrete surface. The significant adsorption-induced retardation on the contaminant penetration into the substrate results in a diffusion-like concentration profile quite different from the shape of the moisture profile. Therefore, the simulations emphasize the importance of adsorption and diffusion on the mass transport of the contaminant and imply that the mass transport driven by capillary flow is not important for the contaminant transport conditions used here.

The dimensionless group $A = (1 - n/n)S\rho_s K_d n_0$ arises naturally from Eq. (9) and can be used to characterize the significance of the adsorption in the process of mass transport. If this dimensionless number is much less than 1, the effect of adsorption is not important, while if this number is much larger than 1, then adsorption/desorption dominates the contaminant transport. In Fig. 3, A = 326, confirming the expected diffusion–adsorption dominated behavior. While it is expected that strong sorption of a contaminant makes it more difficult to remove, one advantage is the surface localization achieved by that process. Of course, here we assume the concrete has a large sorption capacity (implicit in Eq. (8)), which is true for most radiological contaminants. All other simulations (drying process and decontamination) presented in this document always started following this 69-s contamination step. Since this wick-in time is short, we assume decontamination operators do not arrive on the scene until the sample starts to dry.

4.2.2. Step 2: allow contaminant solution to dry for certain amount of time (t_{dry}) (drying step)

At the process time of t = 69 s, the concrete surface begins to dry due to evaporation and continued penetration into the substrate. Contaminant solution inside the substrate was allowed to dry for t_{dry}, after which a decontamination operator applies the HASP layer to begin decontamination. During drying, an evaporative flux equal to $h(S_w - S_{w0})$ was applied at the concrete-air interface ($x = 0$). When $h = 1 \times 10^{-6}$ m/s is applied, the flux simulates an evaporative flux of the order of 1×10^{-7} kg/(m^2 s), which is the evaporation flux measured at an air flow rate of 2 m/s [25]. The zero-flux boundary condition for Cs^+ transport was applied at the concrete/ambient interface during the dry step. Initial values of both saturation and contaminant concentration were the values calculated at the ending point of the previous step, t_{wick}.

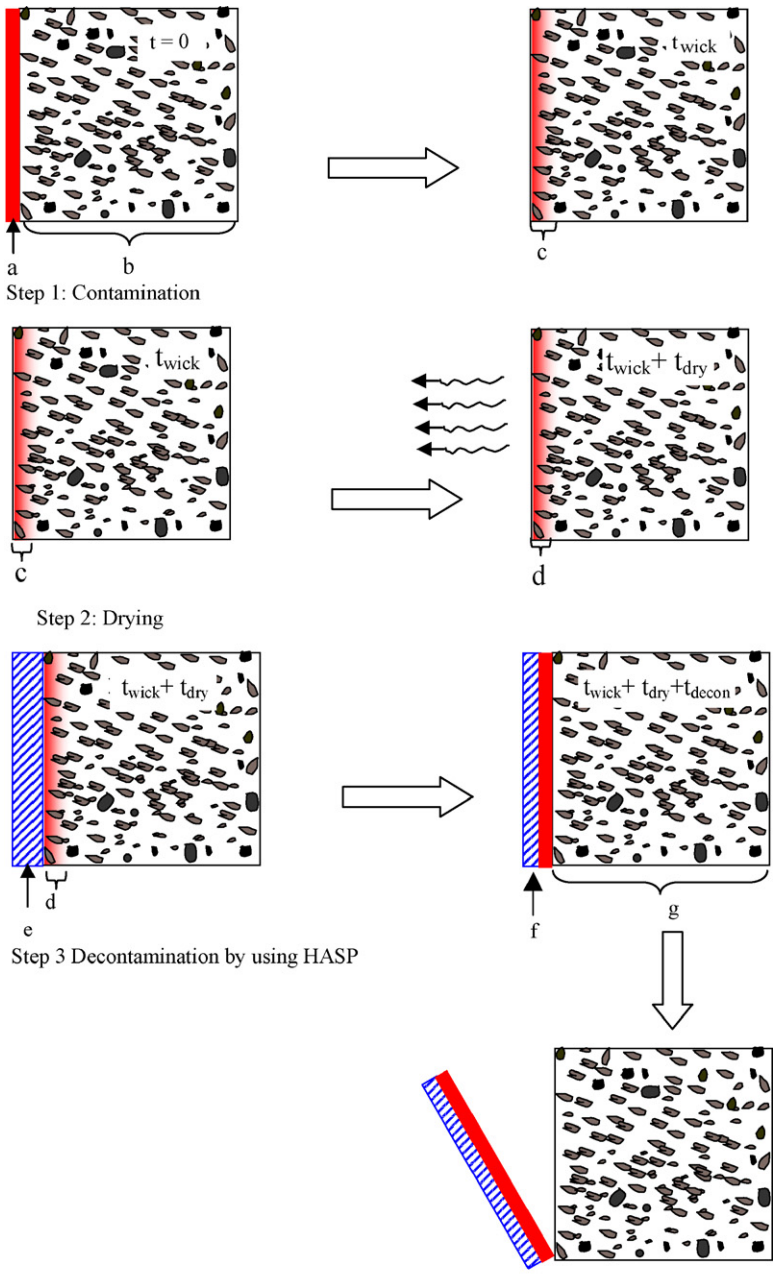

Fig. 2. Schematic of the contamination and decontamination scenario. Step 1: Aqueous phase with dilute Cs^+ contaminant (a) contacts concrete with small residual moisture (b). After a period of t_{wick}, the liquid has wicked into the solid distributing contaminant layer (c). Step 2: the concrete wall dries as it is exposed to ambient for a period of t_{dry}, resulting in a redistribution of the contaminant (d) in the substrate. Step 3: HASP (e) is applied to the concrete surface for a period of t_{decon}. As a result of the decontamination step, contaminant is extracted into the HASP layer, leaving a decontaminated concrete substrate (g) and a cured (solid) HASP layer with enriched contaminant (f). Step 4: the solid HASP layer with enriched contaminant is then stripped and disposed.

Fig. 4 shows the saturation and concentration distribution during the first 30 min of drying. Evaporation at the concrete surface causes a significant drop in moisture near the ambient boundary, though water continues to penetrate into the concrete substrate far from the surface, as illustrated by Fig. 4(a). At the dry time of 1800 s (total process time $t = 1869$ s), about 50% of the moisture that entered the substrate during the contamination step is removed, but the moisture penetration depth is approximately doubled. Fig. 4(b) shows that the rapid decrease of the near-surface saturation does not result in an increase in contaminant solution concentration. Instead, the normalized cesium concentration at the substrate-air interface decreased from 1 to 0.8 in the 30-min dry process due to redistribution deeper into the substrate. Note the shallow penetration of the cesium contaminant compared to the water penetration depth in Fig. 4(a) and (b). The entire concentration distribution falls within the region where water convection is outward toward the surface, yet the contaminant continues to diffuse inward, against the convective flow. This further illustrates the dominance of diffusion–adsorption ($A \gg 1$) for the concrete-cesium system. As a result of this behavior, the differences in experimental

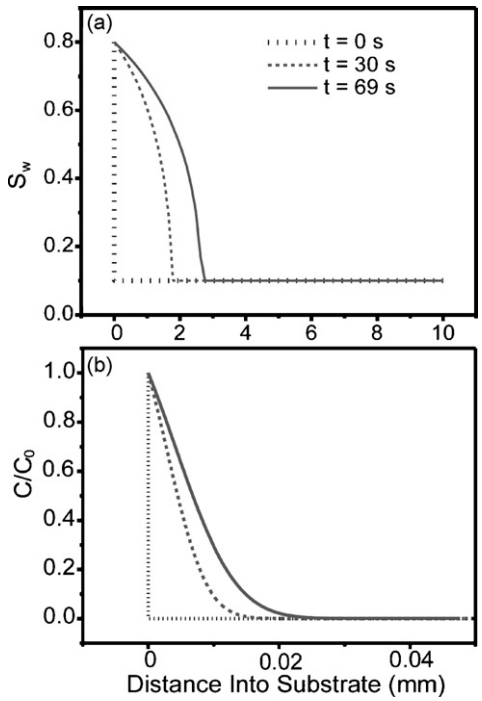

Fig. 3. Evolution of (a) saturation, and (b) normalized concentration profiles in the concrete substrate during the contamination step.

and predicted wicking behavior seen in Fig. 1 are actually rather unimportant for this system. Finally, the implication for a diffusion–adsorption dominated system is that longer dry times (that is, the longer delays before responding to the contamination event) are likely to lower the decontamination efficacy because contaminant moves deeper into the substrate.

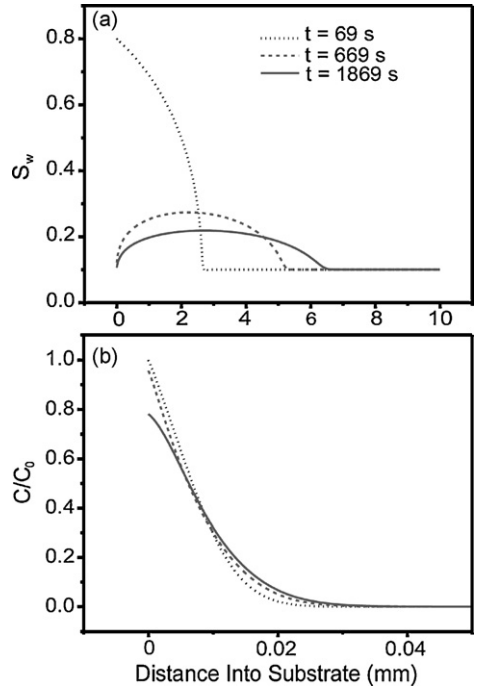

Fig. 4. Evolution of (a) saturation and (b) normalized concentration profiles in the concrete substrate during the drying step.

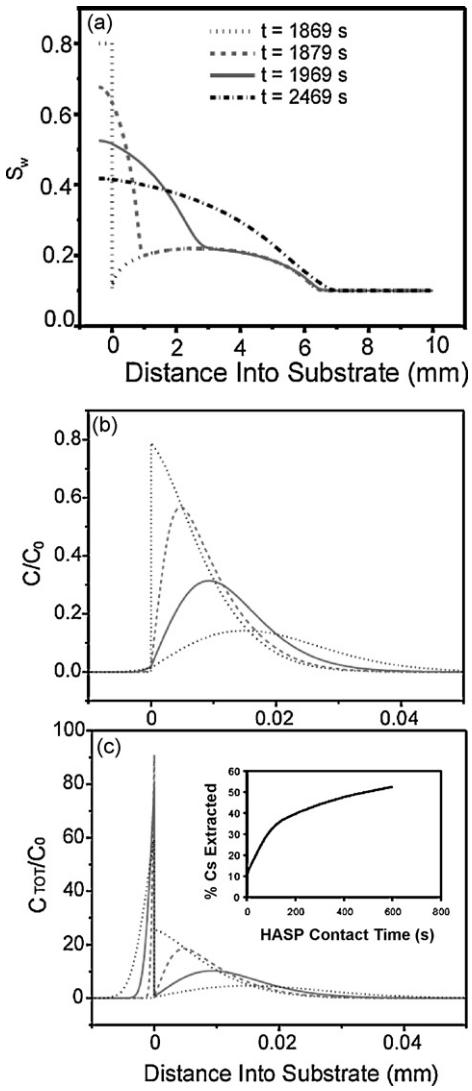

Fig. 5. Evolution of (a) saturation, (b) normalized concentration and (c) normalized total Cs^+ concentration profiles in the concrete substrate ($x > 0$) and the HASP ($x < 0$) during the decontamination step when a no-evaporation BC is applied.

4.2.3. Step 3: apply HASP and allow drying for varying duration (decontamination step)

After a total time $t = t_{wick} + t_{dry}$, decontamination operations begin. After applying a wet HASP coating on the contaminated surface, the operators can choose to either (a) let the HASP coating dry naturally or (b) apply a nonporous outer barrier that slows the drying process significantly. Therefore, at the HASP surface, either an evaporation boundary [$h(S_w - S_{w0})$, $h = 1 \times 10^{-6}$ m/s] or zero flux boundary is applied in this decontamination step. Fig. 5 shows the simulation results for decontamination with an evaporation barrier in place. The HASP is modeled as a porous media with wetting properties identical to concrete. $K_{d,HASP}$ used in the simulations is 1.37 m^3/mol, the HASP porosity is 0.5, and the HASP thickness is 4×10^{-4} m (the average thickness of a HASP layer) unless specified otherwise. Initial moisture saturation in the HASP is set as 0.8, initial Cs concentration within the HASP domain is set to zero. The simulated decontamination period ranges from 10 s to 2 months. For clarity, the longest decontamination time shown in Fig. 5 is 600 s. Initial values of S_w and C in the concrete are those calculated at the ending point of the second step, after drying occurs.

At the beginning of the decontamination process, the saturation inside the substrate is low (smaller than 0.25) as a result of the previous drying process, while the saturation in the wet HASP layer is taken to be 0.8. Therefore, this saturation gradient drives moisture from the HASP layer into the concrete substrate, as shown in Fig. 5(a). Saturation in the HASP layer decreases as decontamination continues and the HASP-layer water flows into the substrate. Inside the concrete substrate, the saturation at the substrate–HASP interface increases to 0.8 immediately upon application of wet HASP coating and then decreases with time due to the further moisture penetration into the substrate.

Fig. 5(b) shows that the application of a HASP layer on the concrete surface causes the Cs^+ concentration at the HASP–concrete interface to drop close to zero immediately. This is due to the facts that HASP has a distribution coefficient higher than that of concrete and it is initially free of contaminant. The total amount of Cs^+ inside the substrate decreases with time as more and more Cs^+ is extracted into the HASP layer via diffusion against the capillary convection into the substrate. Some Cs^+ also diffuses further into the substrate as indicated by the increase of Cs^+ penetration depth and rightward shift of the maximum concentration location. The existence of such inward diffusion is not desirable for building cleanup.

Due to the large $K_{d,HASP}$ value, the solution concentration in the HASP layer is extremely low and the change of contaminant distribution in the HASP layer is hardly shown by solution concentration profiles in Fig. 5(b). Therefore, total cesium concentration (C_{TOT}) is introduced to describe the contaminant distribution inside the HASP. C_{TOT} is defined as the total moles of cesium ions (summation of amount cesium ions adsorbed on surface and dissolved in solution) per unit volume of porous medium:

$$C_{TOT} = CS_w n + CS\rho_s n_0 K_d(1-n) \quad (12)$$

C_{TOT} inside the HASP and substrate is plotted in Fig. 5(c), which clearly shows that the total amount of contaminant in the HASP layer increases with time and, correspondingly, the total amount in the substrate decreases.

The insert in Fig. 5(c) indicates that the longer the HASP contacts the substrate, the more contaminant it removes. Therefore, a long decontamination time might be needed to obtain a satisfactory decontamination result. This figure also shows that the contaminant removal rate is high at the beginning of the decontamination process (over 10% of total Cs^+ was removed in the first 10 s) and the removal rate decreases with time.

4.3. Influence of various process and material parameters

Additional simulations are shown in Figs. 6–8 to further understand the influence of a wider range of operation variables (drying time, HASP contact time, boundary conditions) and material properties (HASP porosity, thickness, and distribution coefficient) on decontamination performance.

We first examine in more detail the role of evaporation at the HASP/air interface on decontamination efficacy. Evaporation is an operating parameter that can be stopped by the application of an impermeable barrier after the HASP layer is applied. When there is no barrier, the evaporation rate is dictated by the ambient conditions such as airflow, temperature, and relative humidity. Fig. 6(a) shows a comparison of the transient remediation with and without evaporation after the contamination step. Fig. 6(b) and (c) are comparable simulations, but allowing for different drying times prior to decontamination (30-min dry in Fig. 6(b) and 151-day dry in Fig. 6(c)).

Since the mass transport of the contaminant by convection is seen to be negligible for the decontamination case studied here, it is not surprising to see that an outward flow created by applying an evaporation boundary at the HASP/ambient interface does not improve decontamination efficacy. Instead, Fig. 6(a)–(c) all indicate that evaporation generally decreases decontamination efficacy by reducing the saturation at the HASP/concrete interface, thereby decreasing the fraction of contaminant in the solution. Since this is an adsorption-dominated case, the removal of the contaminant from the substrate is largely determined by its partition between the solution and the concrete surface. Eq. (12) indicates that the solubilized contaminant is proportional to saturation, while the surface-adsorbed contaminant is independent of saturation. A decrease in saturation leads to the fraction of contaminant in solution decreasing and the contaminant fraction on the surface increasing, if the total amount of contaminant is unchanged. A decrease in the amount of solubilized contaminant leads to a decrease in the contaminant available to be removed by the HASP, resulting in a lower decontamination efficacy.

Fig. 6(a)–(c) also show that the influence of evaporation is negligible when the contact time is short. This is because it takes time for a decrease in saturation at the HASP/air interface to influence the substrate–HASP interface saturation. The delay in response is directly affected by the thickness of the HASP layer and the delay time is longer if a thicker HASP layer is applied.

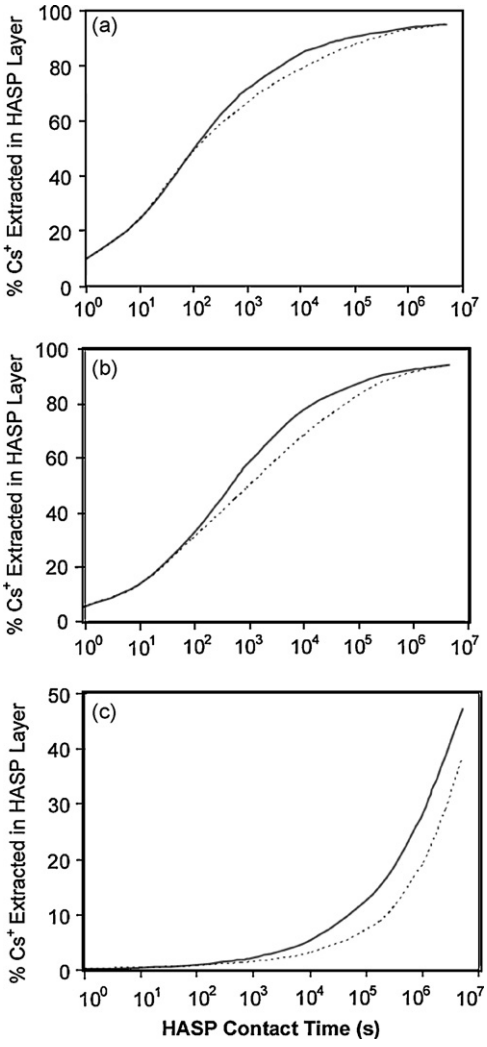

Fig. 6. Influence of evaporation boundary on cesium removal from the contaminated concrete. (a) 0 dry time; (b) 30-min dry time; (c) 151-day dry time; (—) without evaporation; (. . .) with evaporation.

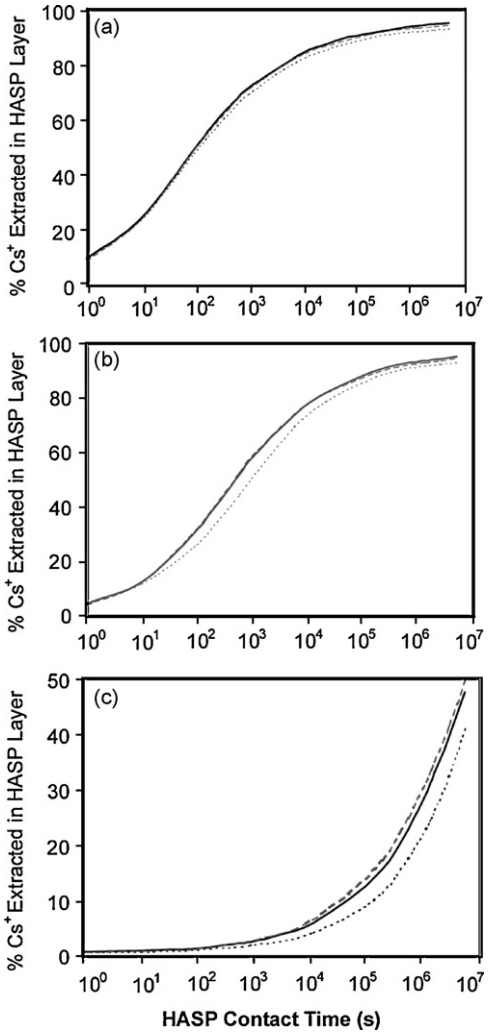

Fig. 7. Influence of HASP layer porosity on cesium removal from the contaminated concrete. (a) 0 dry time; (b) 30-min dry time; (c) 151-day dry time; (. . .) HASP porosity = 0.1; (—) HASP porosity = 0.5; (- - -) HASP porosity = 0.8.

A comparison between Fig. 6(a)–(c) shows that evaporation has a strong impact on the final decontamination efficacy when a long post-contamination dry period is involved. If the dry period is short, the decontamination efficacies both with and without evaporation converge are high after a prolonged (60 days) HASP contact time. If the post-contamination dry period is long, the contaminant removal is difficult, and evaporation decreases the decontamination efficacy significantly. For example, after a 151-day drying period, only 38% Cs^+ is removed through a 60-day decontamination treatment with evaporation (47% Cs^+ is removed when no evaporation is present), while the same amount of Cs^+ can be removed in less than 600 s if only 30-min of drying elapsed prior to decontamination. This is because drying results in less outward diffusion (lower solution contaminant concentration and lower saturation at the HASP/concrete interface) and a deeper contaminant penetration depth. Thus the sooner a HASP coating is applied, the higher the decontamination efficacy.

In short, to achieve a high decontamination efficacy, efforts should be taken to quickly respond to the contamination and vapor barrier should be applied to slow the drying rate of the HASP. The need for a speedy response to enhance decontamination efficacy has been reported by others [29]. Since a no-evaporation boundary condition is desired to achieve good decontamination results under the conditions studied here, the simulation of subsequent factors is performed using a no-evaporation boundary condition.

Fig. 7(a) shows that HASP porosity has little influence on decontamination efficacy when there is no drying step between contamination and the application of a HASP layer, whereas Fig. 7(b) and (c) show that porosity matters when drying is allowed to occur for 30 min or 151 days. A comparison between the three figures indicates that the longer a dry period, i.e., the drier the concrete, the more influence HASP porosity has on decontamination efficacy. Water in the pores of the HASP layer rewets the dried concrete, thereby increasing saturation and solubilizing cesium from the surface. The more porous the HASP coating, the more water that is available to rewet the concrete. The interplay between the amount of pore water available compared to the amount of drying that has taken place, is shown in Fig. 7(b) and (c). Longer post-contamination drying periods increase the influence of HASP porosity, with higher porosities (water contents) yielding higher decontamination factors. This same trend holds for the thickness of the HASP layer applied. Very dry concrete benefits from a thick coating with a high moisture content, though decontamination of wet or moderately wet concrete is unaffected by the thickness of the layer (not shown in figures). Therefore, for the difficult decontamination case where a long dry period is allowed, a thick, high porosity HASP coating is recommended to achieve optimal decontamination.

The most important material property of the HASP with regards to decontamination efficacy is the distribution coefficient ($K_{d,HASP}$). The HASP distribution coefficient should be several orders of magnitude greater than the concrete value in order to drive effective decontamination. Increasing K_d values can be achieved by engineering HASP coating (e.g., including binding sites with stronger affinity to target contaminant(s)). Fig. 8 shows that there is an upper limit on the value of $K_{d,HASP}$ where further increases do not yield improved remediation efficacy. This is true for wet or dried concrete (curves a and b). The reason for this behavior is that the soluble concentration in the HASP layer is so miniscule that it is effectively zero for all practical purposes, and the diffusion driving force is maximized. Theoretically, the maximum Cs^+ removal percentage should approach 100% if $K_{d,HASP}$ is large enough and the system is allowed to reach equilibrium by applying a very long HASP contact time (often an impractically long time).

4.4. Model generalization and broad applications

Heretofore we have focused exclusively on a specific contaminant (cesium) in a specific porous medium (concrete). This can be more broadly generalized by considering the dimensionless

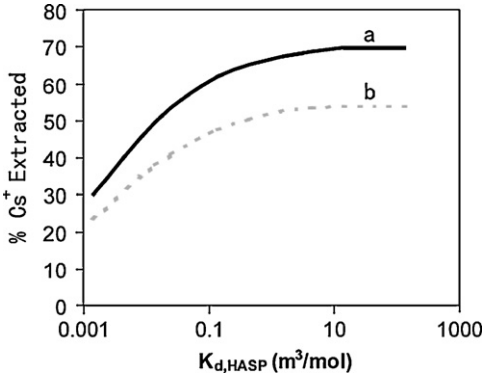

Fig. 8. Influence of distribution coefficient of HASP layer on cesium removal from the contaminated concrete at a HASP contact time of 600 s. (a) 0 dry time; (b) 30-min dry time.

variables:

$$\tilde{t} = \frac{t}{t_{soak}}, \quad \tilde{x} = \frac{x}{\sqrt{D_{C,ave} t_{soak}}}, \quad \text{and} \quad \tilde{V} = \frac{V}{\sqrt{D_{c,ave}/t_{soak}}}$$

which capture the essential diffusion length and time-scales of this process. When substituted into Eq. (9), two dimensionless parameters arise naturally, $A = (1 - n/n)\rho_s S n_0 K_d$ and $B = (D_{C,ave}/D_s)$ in the final dimensionless governing equation:

$$(S_w + A)\frac{\partial C}{\partial \tilde{t}} = -S_w \frac{\partial (C\tilde{V}_w)}{\partial \tilde{x}} + \frac{1}{B}\frac{\partial (S_w^2 (\partial C/\partial \tilde{x}))}{\partial \tilde{x}} \quad (13)$$

As noted previously, the dimensionless number A represents the importance of adsorption in the mass transport process, with large A values indicating strongly adsorbing species–substrate interaction. The dimensionless number B is similar to a Peclet number, which represents the relative importance between convection and diffusion. Eq. (13) suggests that the dimensionless numbers A and B can be used to characterize the mass transport of the contaminant in porous media for various contaminated systems.

Fig. 9 generalizes how various decontamination systems can be characterized by the two dimensionless parameters A and B. The diagram is divided to four regions according to the different dominant mass transport factor(s). Systems with a small A and large B lie in Region 1. The mass transport for such systems is dominated by convection. Systems with a large A and large B lie in Region 2. The mass transport for such systems is dominated by both convection and adsorption. Systems with a small A and small B lie in Region 3. The mass transport for such systems is dominated by diffusion. Systems with a large A and small B lie in Region 4. The mass transport for such systems is dominated by adsorption.

The diagram also shows that each region has inexact boundaries and there are large overlapping areas where two regions meet. In the overlapping areas, the mass transport of the contaminant is also affected by factors other than those lumped in A and B (e.g. duration of the decontamination process, initial and boundary conditions, actual $P_c \sim S_w \sim k_w$ relationships). Therefore actual simulations are needed to determine the dominant mass transport factor(s) in these overlapping areas.

As indicated in Fig. 9, the decontamination results in Figs. 3–8 lie on the edge of Region 4. For concrete with a smaller A (e.g. a smaller specific surface area or a smaller K_d), the system may move from Region 4 to Region 2 and will display more influence of convection and diffusion. For such systems, recommendations for optimizing the decontamination process and HASP development will be quite different from those for adsorption-dominant systems. For example, we have found that decontamination of systems with $A = 3.26$ (edge of Region of 2) are best optimized with thinly applied HASP and no vapor barrier if the response to contamination is fast (e.g. 30 min); however, slow incident responses (e.g. 151-day dry time) would require thickly applied HASP and a vapor barrier to retard evaporation and ensure adequate saturation of the contaminated surface. These effects arise from the increased role of capillary flow when there is a smaller A but the same B as before.

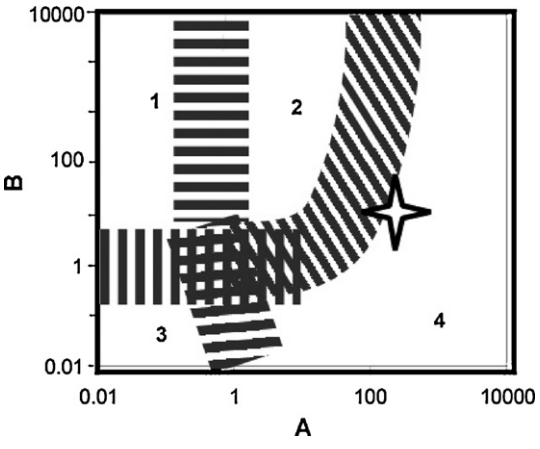

Fig. 9. Contaminated systems are characterized by two dimensionless groupings A and B as defined in the text; Symbol (✧) denotes concrete properties in Figs. 1–8.

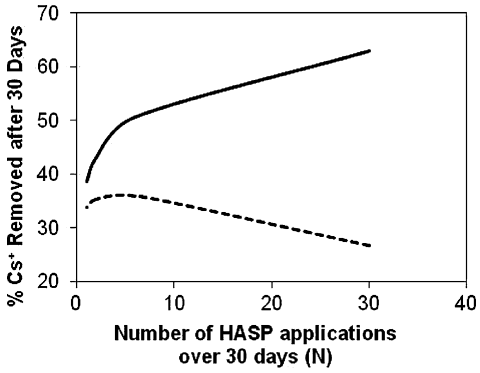

Fig. 10. Cesium removal from two contaminated systems ((—) $A = 326$ and (- - -) $A = 3.26$) after applying multiple applications of fresh HASP in a 30-day decontamination period. All contaminated systems are allowed to dry for 151 days before HASP application, and decontamination process is simulated under no-evaporation boundary condition. $B = 9.5$.

A satisfactory decontamination result can be achieved for high A or low A systems if the post-contamination dry period is short (i.e. response to an event is fast). If the post-contamination dry period is long, decontamination of the small A system is slightly worse owing to the wide dispersion of the contaminant inside the substrate. Extending the HASP contact time is a limited option for contaminated system after a long post-contamination drying process. In order to increase the final decontamination efficacy in a fixed time frame, multiple treatments with fresh HASP should perhaps be considered. Fig. 10 shows the effect of remediation over a total of 30 days when single or multiple applications of fresh HASP are applied during that period (e.g., N applications, with each application extending for $30/N$ days, where $1 \leq N \leq 30$). Also shown is the effect of high A or low A transport conditions. Here we consider the challenging decontamination process associated with a 151-day post-contamination drying period. For a decontamination system with a large A, multiple treatments nearly double the final decontamination efficacy. However, for a decontamination system with small A, going from a single 30-day treatment to five 6-day treatments improves the decontamination process only slightly. Performing more treatments, each for a shorter time, drops the decontamination efficiency significantly. For the small A case, convection has a strong effect on contaminant mass transport, so each HASP application creates an inward flow which carries the contaminant further into the substrate. Although more contaminant will be removed by diffusion after fresh HASP application, much more contaminant penetrates further into the substrate by inward flow when single treatment time is short. Thus, a weak optimum is found for a few reapplications of HASP, where the time is long enough to establish diffusion out, but there is not excessive fresh water convecting contaminant inward.

5. Conclusions

A three-stage contamination–decontamination process was modeled to simulate the removal of the contaminant (Cs^+) from concrete building by applying a HASP coating. Simulation results

show that both the properties of the HASP and operation variables have direct impacts on decontamination efficacy. If the mass transport of the contaminant in the substrate is dominated by adsorption, applying no-evaporation boundary condition to a thick HASP with a large porosity is likely to achieve high decontamination efficacy. If the mass transport of the contaminant in the substrate is dominated by convection, a thin HASP with a low porosity and no vapor barrier is likely to achieve high decontamination efficacy. In addition, multiple decontamination treatments are likely to improve decontamination efficacy effectively for a concrete substrate which absorbs contaminant strongly. For all decontamination systems, HASP with a large distribution coefficient generally achieves better decontamination results. It is also recommended that the HASP should be applied as soon as possible after contaminant exposure. In addition, simulation results show that, counter-intuitively, better decontamination results are sometimes achieved for the contaminated substrates that adsorb contaminant strongly.

More broadly, modeling has proven a valuable tool to gain insights of the whole decontamination process and to guide the process operation and the development of HASP formulations. Simulation of this simple contamination and decontamination scenario provides a basis for future study of more complicated cases.

Acknowledgments

The authors gratefully acknowledge financial support provided by DARPA Radiation Decontamination program, Isotron Corporation; and the Boeing Sutter Endowment for Excellence in Engineering. Work was performed under DARPA Contract HR0011-04-C-0050.

References

[1] D. Elcock, G.A. Klemic, A.L. Taboas, Establishing remediation levels in response to a radiological dispersal Event (or "Dirty Bomb"), Environ. Sci. Technol. 38 (9) (2004) 2505–2512.
[2] A.J. Gonzalez, Security of radioactive sources: the evolving new international dimensions, IAEA Bull. (2001) 39–48, http://www.iaea.org/Publications/Magazines/Bulletin/Bull434/article8.pdf.
[3] J.P. Ring, Radiation risks and dirty bombs, Health Phys. 86 (Suppl. 2) (2004) S42–S47.
[4] I.F. Vovk, V.V. Blagoyev, et al., Technical approaches to decontamination of terrestrial environments in the CIS (former USSR), Sci. Total Environ. 137 (1–3) (1993) 49–63.
[5] M.K. Richmann, D.T. Reed, et al., EXAFS/XANES studies of plutonium-loaded sodalite/glass waste forms, J. Nucl. Mater. 297 (3) (2001) 303–312.
[6] M. Bailo, L.E. Boing, et al., State of the art technology for decontamination and dismantling of nuclear facilities, International atomic energy agency (IAEA), Vienna, 1999, http://www-pub.iaea.org/MTCD/publications/PDF/TRS395_scr/D395_Part1_scr.pdf.
[7] G.A. Fox, V.F. Medina, Evaluating factors affecting the permeability of emulsions used to stabilize radioactive contamination from a radiological dispersal device, Environ. Sci. Technol. 39 (10) (2005) 3762–3769.
[8] DARPA Contract Number: HR0011-04-C-0050, Advanced strippable coatings technology, Isotron Corporation.
[9] H.L. Lomasney, J.G. Grawe, V.K. Sheth, In situ polymeric membrane for isolating hazardous materials, United States Patent No. 4,632,847 (1986).
[10] S.M. Haight, D.T. Schwartz, M.A. Lilga, In-situ oxidation state profiling of nickel hexacyanoferrate derivatized electrodes using line imaging Raman spectroscopy and multivariate calibration, J. Electrochem. Soc. 146 (1999) 1866–1872.
[11] K.M. Jeerage, D.T. Schwartz, Characterization of cathodically deposited nickel hexacyanoferrate for electrochemically switched ion exchange, Sep. Sci Technol. 35 (2000) 2375–2392.
[12] K.M. Jeerage, W.A. Steen, D.T. Schwartz, Charge-density-dependent partitioning of Cs^+ and K^+ into nickel hexacyanoferrate matrices, Langmuir 18 (2002) 3620–3625.
[13] W.A. Steen, D.T. Schwartz, A route to combinatorial libraries of electroactive nickel hexacyanoferrate, Chem. Mater. 15 (2003) 2449–2453.
[14] T. Okumura, T.E. Graedel, The contemporary materials cycle for radioactive 137Cs in the United States, Health Phys. 90 (6) (2006) 521–532.
[15] M.T. Harris, D.W. DePaoli, M.R. Ally, Modeling the electrokinetic decontamination of concrete, Sep. Sci. Technol. 32 (1–4) (1997) 827–848.
[16] A. Jakob, F.A. Sarott, P. Spieler, Diffusion and Sorption on Hardened Cement Pastes—Experiments and Modeling Results, Switzerland, 1999, pp. 1–194.
[17] J. Bear, Y. Bachmat, Introduction to Modeling of Transport Phenomena in Porous Media. Theory and Applications of Transport in Porous Media, Kluwer Academic Publishers, Dordrecht, 1991.
[18] A.T. Corey, Interrelation between gas and oil relative permeabilities, in: Pennsylvania State University, 18th Technical Conference on Petroleum Production, Mineral Inds. Expt. Sta. Bull., No. 64, 1954, pp. 29–35.
[19] T.N. Narasimhan, P.A. Witherspoon, A.L. Edwards, Numerical-model for saturated-unsaturated flow in deformable porous-media. 2. Algorithm, Water Resour. Res. 14 (2) (1978) 255–261.
[20] G. Mayer, F. Jacobs, F.H. Wittmann, Experimental determination and numerical simulation of the permeability of cementitious materials, Nucl. Eng. Des. 138 (2) (1992) 171–177.
[21] R. Lucas, Rate of capillary ascension of liquids, Kolloid-Zeitschrift 23 (1918) 15–22.
[22] E.W. Washburn, Dynamics of capillary flow, Phys. Rev. 17 (1921) 374–375.
[23] W. He, J.S. Yi, T. Van Nguyen, Two-phase flow model of the cathode of PEM fuel cells using interdigitated flow fields, AIChE J. 46 (10) (2000) 2053–2064.
[24] Z.H. Wang, C.Y. Wang, K.S. Chen, Two-phase flow and transport in the air cathode of proton exchange membrane fuel cells, J. Power Sources 94 (1) (2001) 40–50.
[25] F.J. Trujillo, S.J. Lovatt, et al., CFD modeling of the heat and mass transfer process during the evaporation of water from a circular cylinder, in: Third International Conference on CFD in the Minerals and Process Industries, Melbourne, Australia, 2003.
[26] J.L. Conca, J. Wright, Diffusion coefficients in gravel under unsaturated conditions, Water Resour. Res. 26 (5) (1990) 1055–1066.
[27] J. Real, F. Persin, C. Camarasa-Claret, Mechanisms of desorption of 134Cs and 85Sr aerosols deposited on urban surfaces, J. Environ. Radioact. 62 (1) (2002) 1–15.
[28] O. Truc, J.P. Ollivier, L.O. Nilsson, Numerical simulation of multi-species transport through saturated concrete during a migration test—MsDiff code, Cem. Concr. Res. 30 (10) (2000) 1581–1592.
[29] K.G. Andersson, J. Roed, A Nordic preparedness guide for early clean-up in radioactively contaminated residential areas, J. Environ. Rad. 46 (1999) 207–223.